CHEMPHYSCHEM

DOI: 10.1002/cphc.201000487

What Happens Inside a Fuel Cell? Developing an Experimental Functional Map of Fuel Cell Performance

Daniel J. L. Brett,*[a] Anthony R. Kucernak,*[b] Patricia Aguiar,[c] Stephen C. Atkins,[b] Nigel P. Brandon,[c] Ralph Clague,[c] Lesley F. Cohen,[d] Gareth Hinds,[e] Christos Kalyvas,[b] Gregory J. Offer,[c] Bradley Ladewig,[f] Robert Maher,[d] Andrew Marquis,[g] Paul Shearing,[c] Nikos Vasileiadis,[c] and Velisa Vesovic[c]

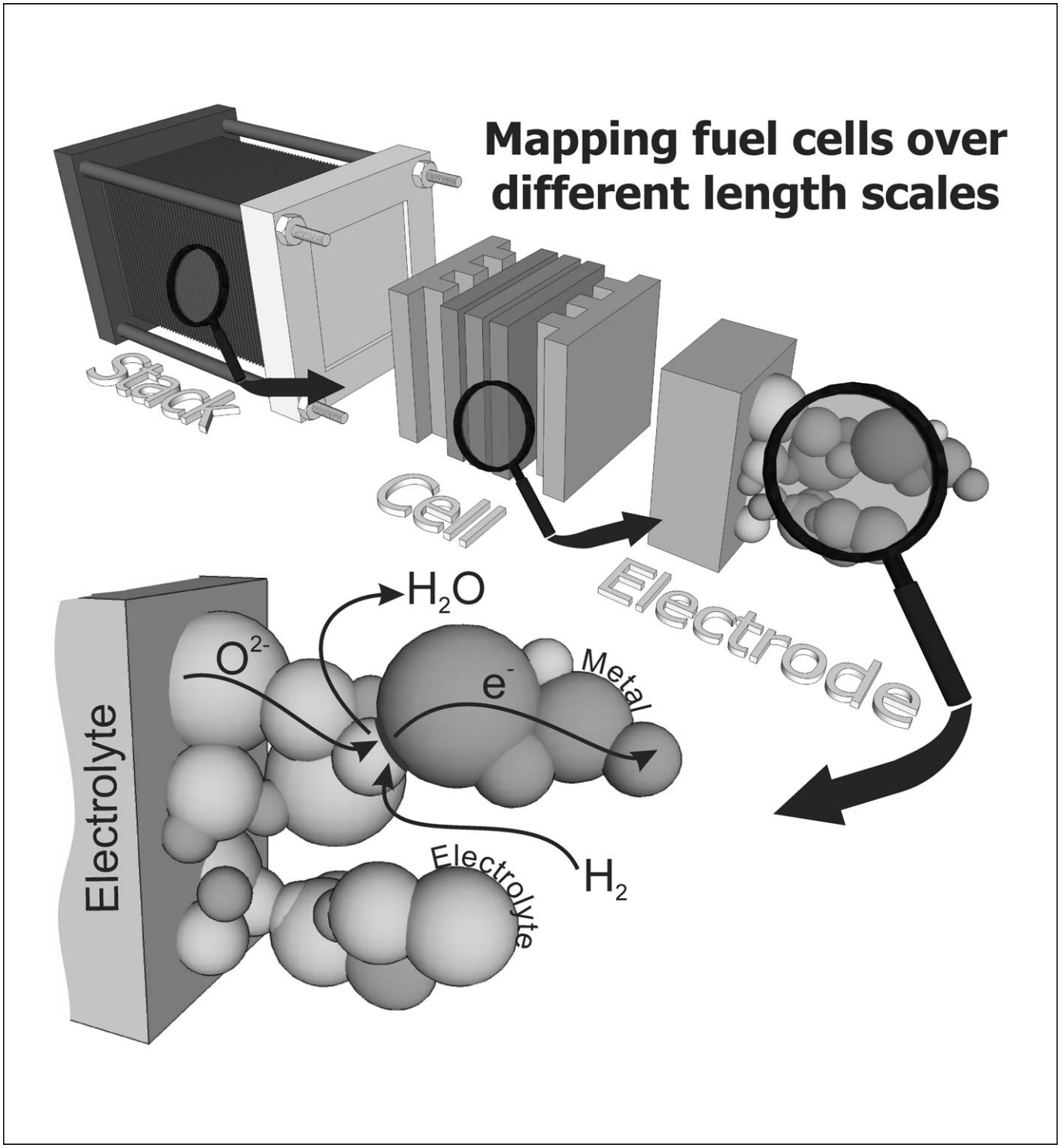

Fuel cell performance is determined by the complex interplay of mass transport, energy transfer and electrochemical processes. The convolution of these processes leads to spatial heterogeneity in the way that fuel cells perform, particularly due to reactant consumption, water management and the design of fluid-flow plates. It is therefore unlikely that any bulk measurement made on a fuel cell will accurately represent performance at all parts of the cell. The ability to make spatially resolved measurements in a fuel cell provides one of the most useful ways in which to monitor and optimise performance. This Minireview explores a range of in situ techniques being used to study fuel cells and describes the use of novel experimental techniques that the authors have used to develop an 'experimental functional map' of fuel cell performance. These techniques include the mapping of current density, electrochemical impedance, electrolyte conductivity, contact resistance and CO poisoning distribution within working PEFCs, as well as mapping the flow of reactant in gas channels using laser Doppler anemometry (LDA). For the high-temperature solid oxide fuel cell (SOFC), temperature mapping, reference electrode placement and the use of Raman spectroscopy are described along with methods to map the microstructural features of electrodes. The combination of these techniques, applied across a range of fuel cell operating conditions, allows a unique picture of the internal workings of fuel cells to be obtained and have been used to validate both numerical and analytical models.

1. Introduction

Fuel cells hold great promise as a clean energy-conversion technology. The range of potential applications includes small portable electronic devices, power sources for vehicular transport and residential combined heat and power (CHP) supplies. The market for these applications is very large, and widespread adoption should lead to a reduced dependence on fossil fuels and encourage the development of a "hydrogen economy".

Fundamental to the development of the basic stack technology is a range of appropriate diagnostics, which allow for the detailed observation and measurement of the phenomena occurring in operating fuel cells. These diagnostics can be classified into two broad groupings: those that treat the cell (or stack, depending on the test configuration) as a homogeneous unit, and those that take into account the heterogeneous distribution of the numerous factors which affect the performance. These factors include, but are not limited to, reactant temperature, pressure, humidity, velocity and concentration; localised current and potential; catalyst loading and poisoning; contact resistance and membrane conductivity. While it is generally accepted that variations in these and other factors have a large impact on fuel cell behaviour, the diagnostics are not always available to quantify them. Indeed, crude bulk measurements of fuel cell performance can be misleading when the performance of a fuel cell is spatially heterogeneous.

This article begins with a review of the range of in situ diagnostics techniques reported in the literature and continues with a synopsis of the suite of methods developed by the authors to examine the internal workings of both the low-temperature polymer electrolyte fuel cell (PEFC), which operates around 80 °C, and the high-temperature solid oxide fuel cell (SOFC) operating in excess of 500 °C. A brief description of work we are doing to map the microstructure of SOFC electrodes is also included.

[a] *Dr. D. J. L. Brett*
The Centre for CO_2Technology
Department of Chemical Engineering, UCL
London (UK), WC1E 7JE
Fax: (+44) 20-7679-3310
E-mail: d.brett@ucl.ac.uk

[b] *Prof. A. R. Kucernak, S. C. Atkins, Dr. C. Kalyvas*
The Department of Chemistry, Imperial College London
SW7 2AZ, London (UK)
Fax: (+44) 20-7594-5831
E-mail: anthony@imperial.ac.uk

[c] *Dr. P. Aguiar, Prof. N. P. Brandon, Dr. R. Clague, Dr. G. J. Offer, Dr. P. Shearing, Dr. N. Vasileiadis, Dr. V. Vesovic*
The Department of Earth Science and Engineering
Imperial College London, London, SW7 2AZ (UK)

[d] *Prof. L. F. Cohen, Dr. R. Maher*
The Department of Physics
Imperial College London, London, SW7 2AZ (UK)

[e] *Dr. G. Hinds*
Materials Division, National Physical Laboratory
Teddington, Middlesex, TW11 0LW (UK)

[f] *Dr. B. Ladewig*
The Department of Chemical Engineering
Monash University, Victoria, VIC 3800, Australia

[g] *Dr. A. Marquis*
The Department of Mechanical Engineering
Imperial College London, SW7 2AZ, London (UK)

2. Methods of Analysing Fuel Cells

2.1. Electrical Techniques

Contact Resistance

Ohmic losses within fuel cells constitute a significant performance limitation. Electrical contact resistance between the gas diffusion layer (GDL) and the ridges of the flow-field plate (called "lands") is a major source of this Ohmic loss. The clamping pressure applied to the fuel cell is known to have an effect on the contact resistance and the diffusion properties of the GDL—this pressure decreases contact resistance but also compresses the GDL, leading to a lower porosity. Construction of a fuel cell/stack must consider the method by which it will be held together and the force used to do this. The way in which a fuel cell is put into compression has been shown to have an effect on its performance.[1,2]

The optimum method of clamping a cell/stack has not been adequately reported in the literature. Methods such as hydraulic jacks, pneumatic presses and sprung screws have been used, but the most common method of clamping uses tie-rods/bolts which compress the end-plates of the cell/stack to-

gether. The number and positioning of the rods has no particular statute. The method suffers from irreproducibility due to poor control of the clamping pressure and the order in which the tie-rods are tightened. Although the torque on each bolt can be accurately controlled, it is not a direct measure of the clamping pressure, because each component of the fuel cell will compress to a different degree, and account for a certain amount of the compaction force. Pressure-sensitive "paper" (such as PRESSUREX produced by Sensor Products, USA) can be incorporated into the stack and gives a good measure of the pressure distribution; however, the cell or stack must be disassembled to develop the sheet. Other ways in which variation in the contact resistance can occur within the cell include component thickness variation, reactant gas pressure variation, positioning and type of gasket used, flow-field geometry and even membrane swelling (Nafion has been measured to swell up to 22% of its original size upon hydration[3]). Such irreproducibility of the clamping conditions is a major factor that hampers making accurate comparative studies of membrane electrode assembly (MEA) performance.

Studies have been presented that have looked at the Ohmic losses in PEFCs. A method in which voltage measuring probes are inserted at different points in the MEA composite has been used to deconvolute the electronic component of the Ohmic losses in the GDL and flow-field plate from the ionic component of the Ohmic losses in the membrane.[4] This method has been used to study the effect of flow-field plate materials and compression force on the contact resistance. It was found that an increase in the clamping pressure leads to a decrease in the contact resistance. The electrode material and its pre-treatment also has a decisive effect on contact resistance and has been found to vary with time, the current flowing and whether the electrode is the anode or cathode.[5–8]

The effect of the compression force on the performance of a PEFC has been studied in terms of the effect of pressure on the GDL. Lee et al. demonstrated that an optimum compression force exists depending on the type of GDL used (Toray, CARBEL, ELAT and combinations thereof).[1] An increased clamping pressure was found to decrease Ohmic loss, but also decrease the porosity of the GDL, resulting in mass-transport limitations at higher current densities. It was also found that excessive clamping pressure can cause irreversible damage to the GDL. These findings have been emphasised by work that showed how over-compression leads to a dramatic reduction in the performance of a direct methanol fuel cell (DMFC).[9] This was found to be due to morphological impairment of the GDL, resulting in encumbered reactant transport and deleterious effects on its water management properties. Localised current mapping has also shown clamping pressure to have a strong effect on the spatial distribution of current.[2]

These studies show that compression of the GDL modifies its physical properties. Work has been presented that aims to identify the optimum material, porosity and hydrophobicity for a GDL.[10–12] However, all of these parameters will be affected when subject to compression. The effect of clamping pressure on the contact electrode/bipolar plate material has been studied. Hentall et al. found that when Grafoil is used as the current collector, an optimum compression force exists that will produce the maximum power output.[13]

Current Mapping

Improvements in fuel cell components and system design can only be gauged by following comprehensive and formalised testing procedures. One of the most telling ways in which fuel cell performance can be gauged is by in situ current mapping. A range of approaches has been applied to achieve current mapping. The ideal requirements of a current-density mapping technique are: high spatial resolution; real-time measurement to capture transient response (<1 s sampling intervals); dynamic control of cell potential and total cell current to compose localised polarisation plots; no detrimental effects to the MEA (i.e. no segmentation or modification of the GDL, catalyst or membrane); applicability to a wide range of flow-field designs, such that it interacts with the MEA in a similar way to that in the normal configuration; correction of lead, connect and contact resistance, such that all voltage losses are compensated for; equal applicability to the anode and cathode.

The challenge of making localised current-density measurements comes mainly from the fact that the measurement must be made at various positions on a GDL material that has a very low lateral electronic resistivity and a relatively higher through-plane resistivity (Toray paper TGP-H has an in-plane and through-plane resistivity of $\approx 5\,m\Omega\,cm$ and $\approx 70\,m\Omega\,cm$, respectively). This means that whatever the method used to draw the current away from each location, it should not present any resistive or electrical potential variation, since this would result in lateral flow of current down a potential gradient or via the route of minimal resistance. Such a situation will lead to a non-representative current distribution. Of course, such conditions can be expected in a fuel cell run in the conventional mode; variations in the GDL or flow-plate bulk resistance or contact resistance will cause a lateral current to flow. However, when performing current density mapping experiments, such factors will usually be assumed to be constant and evenly distributed so that current density variations associated with the operating conditions can be focused on.

Natarajan and Nguyen have studied the effect of electrode configuration on current-distribution measurements.[14] Difference in contact resistance between different current collector segments was found to be responsible for inferior performance in constant voltage mode compared to constant current mode, thus emphasising the need for contact resistance compensation. Eckl et al. have modelled the uncertainty introduced in making current-distribution measurements due to lateral currents for different current-mapping approaches.[15]

Work by Rieke and Vanderborgh provides an early example of attempts to map current-density distribution.[16] This method used a photolithographic technique to fabricate an array of counter and reference electrodes directly onto the membrane electrolyte. Such an array of microelectrodes, used with a single working electrode and operating in a half-cell configuration, allows localised measurement of both current and potential. However, the technique suffered with reference

electrode irreproducibility and operation was not in a normal fuel cell configuration.

The effect of the Ohmic resistance of the GDL on the current and potential distribution was first demonstrated in work by Vermeijlen et al.[17] This study highlighted the need for adequate and uniformly distributed current collection from the electrode surface and showed that higher bulk current density leads to a more heterogeneous current distribution across an electrode, a feature observed in several current-distribution studies.

Stumper et al. investigated the current distribution at low resolution within a working fuel cell by segmenting the MEA into three sub-cells.[18] The study was made on a full 2D flow-field plate and separate measurements were obtained at the "inlet", "middle" and "outlet" of the cell. Each electrical connection to the cell is isolated from the others due to the segmentation of the MEA and discrete current sampling points were made by punching out 10 mm diameter sections of the anode and cathode. Each sub-cell is controlled with its own load circuit and potential sense lines were used to correct for voltage drop in the supply lines. It was found that the downstream parts of the flow-field suffered from decreased current density at high overpotentials due to decrease in reactant concentration. In a more advanced configuration, the current density was sampled at 121 points across the cell (MEA non-segmented). This was performed using a passive resistor network, across which the potential drop is measured to provide a value of the current at that point. This method allows high spatial resolution and real-time current measurement. However, it does not correct for variation in contact resistance and will be prone to lateral current flow (especially at high current densities) unless the tolerance of the resistor network can be guaranteed to a very high level, or the resistance of the shunt is significantly less than the lateral resistance of the GDL.

A system developed by Cleghorn et al. used a method of current distribution based on segmented electrodes fabricated using printed circuit board (PCB) technology.[19] Two electronic load circuits are used in conjunction with a switch box to cycle through 18 discreet contacts, with one load associated with the contact under test and the other associated with the remaining 17 contacts. This technique has the substantial advantage of being able to perform localised resistance measurements, particularly useful for studying water management in the cell. However, the method is not capable of making real-time measurements and collection of localised polarisation curves is more convoluted, no correction for contact resistance is made.

An alternative method has been proposed by Wieser et al.[20] based on an array of magnetic loop (Hall Effect) sensors. This technique has the key advantage that the method of current measurement is non-intrusive, that is, there is no need for separate loads or shunt resistors that increase the chance of lateral current flow. Positions on the flow-field plate at which current measurements are to be taken are chosen and the current drawn off at that point is measured with the Hall sensor. This technique allows real-time measurements to be made and MEAs can be tested without modification. However, the method does not account for differences in the contact resistance between contact and MEA at each measurement point; the spatial resolution is also limited by the size of the sensor (≈38 mm×38 mm). Results using the same technique have been published by Yoon et al.[21] Analysis of a full 2D cell provided evidence for current limitation due to catalyst flooding towards the end of the cell/flow channel length (under conditions of extreme reactant humidification) and drying towards the start of the channel at lower reactant humidification.

A significant contribution has been made to the field of localised measurements and in situ diagnostics by workers at the Helsinki University of Technology.[22–25] This group's approach is similar to that of Stumper et al.[18] in that an array of shunt resistors (48×0.1 Ω) is used to ascertain the current distribution, in this case of a free-breathing cathode PEFC (5 cm× 5 cm flow-field). In this technique, some additional control is obtained by the ability to adjust the contact pressure of each of the contact electrodes in turn. However, this does not correct for the contact resistance per se. Detailed 2D plots of the current distribution under different load conditions and temperatures and under conditions of forced and free convection provide unique insight into the distinctive operation of a free-breathing system.[22] The same system was also used to investigate the distribution of mass-diffusion overpotentials using a flow pulse method. It was shown that localised cell resistance can also be derived from current interrupt measurements.[23]

Other leaders in this area include Mench et al. at Penn State who have, for example, examined the current distribution within a DMFC consisting of ten contact electrodes.[26,27] Each of the contacts was controlled using a commercially available battery/fuel cell test system, effectively a multi-channel potentiostat. This system affords real-time data collection and can be applied to off-the-shelf MEAs. The fuel cell used in this study is specially designed to facilitate in situ diagnostics, being fabricated from transparent material and having localised sample ports for reactant/product species sampling.

Recent examples of new innovation in current-distribution measurements include: Sun et al. who used a specially designed measuring gasket inserted between the GDL and flow-field plate;[28] combination of current mapping with complementary techniques such as localised temperature measurement and water distribution;[29] measuring current distribution with sub-millimetre resolution;[30] indirect evaluation of current densities by measuring the locally induced magnetic field[31] and comparison between current density distribution obtained using magnetotomography and the segmented cell approach.[32]

Generally, current-distribution measurements have been very useful for studying the effect of cell temperature, reactant flow rate, humidification, reactant pressure and fuel cell transients.[33–39]

Electrochemical Impedance

One of the most insightful ways in which fuel cells can be analysed is by making electrochemical impedance spectroscopy (EIS) measurements. This technique has been applied to all va-

rieties of fuel cells,[40] as well as studies aimed specifically at PEFCs.[41–47] This alternating-current technique complements direct-current measurements by providing a new dimension of information. Impedance measurements furnish values of membrane resistance, kinetic and mass-transport information. Since these parameters are expected to change depending on the electrical load, it is important that these measurements can be made over the power range of the fuel cell. One limitation to the application of EIS to larger fuel cells is that the bandwidth of most commercial electronic loads operating at high currents is not large enough to encompass the high-frequency (kHz) features.

A fundamental limitation of conventional EIS when applied to fuel cells is that the measurement is performed on the entire cell, that is, the fuel cell is treated as a two-terminal device. Truly representative measurements can only be obtained if the fuel cell is operated under a mode in which local conditions are invariant within the fuel cell, that is, that there is an even distribution of reactant and current density. In reality, such a mode of operation will rarely be encountered. One way in which this leads to inaccurate interpretation of EIS results is in the choice of the equivalent circuit with which the data is analysed. Various equivalent circuits have been proposed to represent PEFC operation, ranging from simple four-component circuits to more complicated transmission-line representations.[48] The problem when choosing an equivalent circuit is that it must suit the bulk EIS result; when in actual fact different parts of the fuel cell may be fit to the equivalent circuit with very different parameters, or may require a different equivalent circuit altogether. Thus, knowledge of the way in which impedance characteristics vary should in itself lead to improved equivalent circuit selection.

Brett et al. have demonstrated fuel cell localised electrochemical impedance spectroscopy (FC-LEIS)[49] and have used the technique to map electrolyte membrane resistance under a wide range of operating conditions. Hakenjos and Hebling have demonstrated localised impedance measurements[50] and Schneider et al. have simultaneously combined localised impedance and neutron radiography measurements;[51] these two techniques being particularly powerful when used in unison since the location of water and its impact on electrolyte hydration can both be characterised. Incorporation of miniature temperature/humidity sensors in flow-plates to study water management under load has been particularly useful in this regard.[52]

2.2. Non-Electrical Techniques

Neutron Imaging

Water plays a critical role in determining the performance of PEFCs.[53] In order for the electrolyte membrane to have suitable proton conductivity, it must be adequately hydrated. Even though water is a product of the fuel cell reaction, it is still usually necessary to humidify the reactant feed to avoid drying of the membrane. However, too much water can lead to 'flooding' of the cell, which impedes reactant access to the catalyst. It is therefore necessary to understand how water is generated and how it is distributed around the system to ensure an effective water balance. Neutron radiographical measurements are particularly effective for investigation of water distribution in PEFCs due to the high sensitivity of the technique to hydrogen-containing molecules. Rosdale et al. pioneered the use of small angle neutron scattering (SANS) to study the internal structure of the electrolyte membrane, depending on its water content.[54] Bellows et al. also showed how neutron attenuation can be used to profile water gradients through the thickness of membranes in operational cells.[55] However, a relatively thick membrane of 500 μm was required to build the profile with a spatial resolution of 40 μm.

Kramer et al. have used neutron imaging to study the distribution of water in flow channels and the GDL, and have shown how different flow-channel geometries result in different water-accumulation patterns.[56] They have correlated neutron imaging with localised electrochemical impedance measurements[57] and shown how different materials affect water-droplet formation.[58] Similarly, workers at Penn State have used the technique to study the formation of water in channels (this being particularly noticeable at 90° bends in the channel)[59,60] and the effect of the diffusion-layer material on water storage, distribution and removal.[61]

Satija et al. have demonstrated both real-time radiography of a working fuel cell showing water production, transport and removal from a working PEFC with 2 s resolution and 3D tomography of a dry cell that can be used to screen for structural defects.[62]

Neutron radiography techniques are proving to be an extremely powerful tool for the non-destructive characterisation of working fuel cells, particularly with respect to water management. Further enhancements to the technique are possible through improvements in the spatial and temporal resolution as well as data processing. The major limitation to the uptake of the technique is the requirement for a neutron source.

Spectroscopic Techniques

Unique insight into the operation of working PEFCs has been gained by the application of various spectroscopic techniques. Fibre-optic fluorescence spectroscopy has been used to detect changes in the water content of Nafion under different operating conditions.[63] Diode laser based absorption spectroscopy has been used to measure water partial pressure in the flow channels of a modified bipolar plate with an accuracy of 10%.[64,65] Spin trap electron paramagnetic resonance has been used to study membrane degradation[66] and FTIR methanol oxidation on Pt under operational fuel cell conditions.[67] The feasibility of using confocal Raman spectroscopy has been demonstrated for making semi-quantitative measurement of the distribution of water through the thickness of a Nafion 117 membrane at varying current densities[68] and Feindel et al. have shown that 1H NMR microscopy can also be used to map water distribution in a working cell.[69] Interesting results have been reported from workers at the Tokyo Institute of Technolo-

gy, who used magnetic resonance imaging (MRI) to map water distribution within an MEA with a resolution of 25 μm.[70–72]

Optical Techniques

Fluid flow within a flow-field plate can be investigated using flow-visualisation techniques. For example, a coloured dye can be injected into the flow-fluid and monitoring the distribution of the dye can be monitored with a CCD camera through a transparent window. This form of flow visualisation is limited to a liquid feed; however, the flow rate of the liquid can be adjusted to have the same Reynolds number as that of a gas and therefore simulate the flow of a gaseous reactant. Areas of turbulence and laminar flow can be readily determined and the procedure for performing the test is relatively simple. A similar approach has been used to investigate the effect of the GDL on the flow distribution in different flow geometries.[73] Visual inspection has been used by Tüber et al. to investigate the effects of two-phase flow and flooding within a fuel cell under conditions of varying air stoichiometry and temperature.[74] These results show that the relatively simple facility of visual inspection of water build-up within the channel and GDL can go a long way in reconciling the association between current generation and water management.

Flow within a working DMFC has been studied using a similar form of visual visualisation.[75] Since the cell was operational, bubbles of CO_2 were observed to form as a by-product of the methanol oxidation; the bubbles seed the fluid and give an impression of flow (without the need of a dye) as well as an indication of the extent of reaction at the point of formation.

Other optical studies of fuel cells include the monitoring of flooding in flow channels,[76] liquid water and ice formation during start-up from sub-zero temperatures[77] and bubble dynamics in DMFCs.[78,79]

Visual inspection of flow is largely confined to liquids, some information can be obtained regarding water production, transport and condensation in channels but seeding the flow for flow visualisation is difficult without affecting the performance of the cell. One method of flow characterisation that the authors have employed and has been reported by others, is the technique of laser Doppler anemometry (LDA).[80,81] This technique has been applied extensively to the study of flow in systems such as the internal combustion engine and works by focusing a laser beam into a flow channel and measuring the scattered light from particles used to seed the flow. Information on the speed and direction of the flow can be obtained and almost the entire cross-section of a channel or corner can be profiled. Such a technique could potentially prove extremely useful in flow-field plate design.

Temperature Mapping

Incorporation of temperature sensors (i.e. thermocouples and thermistors) is necessary for proper control, test and operation of fuel cells. This ranges from the crude placement of a single sensor to highly instrumented arrangements that allow 2D mapping of a single cell in conjunction with current mapping[82] or plate-by-plate profiling of stacks.[83]

To get an accurate measure of the temperature of a cell and detect temperature changes as they happen at the electrode, it is necessary to place the sensor as close to the electrodes (or electrolyte) as possible. Incorporation of conventional thermocouples close to the interface of the current collector and electrode may lead to membrane penetration; to avoid this, thin-film temperature sensors have been developed that allow in situ measurement within the membrane electrolyte.[84]

An alternative to discreet temperature sensors is the use of infrared (IR) measurements. This technique has the advantage of not requiring sensor placement or connecting leads and high spatial resolution and frame collection rates can be achieved. The technique is ideal for measuring the outer-surface temperature of a fuel cell or stack. However, in order to investigate the temperature within a fuel cell, the construction needs to be modified to allow optical access to the surface of interest (i.e. electrode surfaces).

Infrared thermal imaging has been performed on PEFCs using IR transparent windows made from zinc selenide (>75% transmission over 8–12 μm)[85] and barium fluoride (>85% transmission over 8–12 μm, although a correction was still performed).[86] These studies showed that significant temperature variation results across the surface of a PEFC due to variation in current density, humidification and reactant composition. The work of Wang et al.[86] demonstrates how the electrode-surface temperature increases with the current density. For a current density of 1.38 $A\,cm^{-2}$, a maximum spatial distribution of about 6 °C was observed over the 2.9×3.9 cm electrode surface, with over 10 °C temperature rise recorded in some parts of the electrode. The results show that it is important to have a measure of the temperature at the electrode of the fuel cell since the bulk fuel cell temperature and electrode temperature can vary significantly (over 8 °C in this study). In addition, it was found that a significant time was necessary for the electrode to reach a stable temperature after a current step change. Over 1800 s was required in this instance in order for the heat generated to radiate through the test cell to the environment.

3. Experimental Approach

To gain a more in-depth understanding of fuel cell operation, a suite of techniques has been developed by the authors that examine performance in relation to each component of the fuel cell. Figure 1 summarises the range of measurements that have been performed for the PEFC. The processes examined include electrolyte-resistance mapping, distribution of carbon monoxide on the surface of the electrocatalyst, current-density mapping, discrete measurements of the contact resistance between the gas diffusion layer and the lands of flow-field plates and imaging of reactant flow velocity in the channels of the flow-field plates.

To examine the gas flow in the channels of PEFCs, an optically transparent fuel cell was constructed such that LDA could be applied. For the rest of the PEFC techniques, a fuel cell was

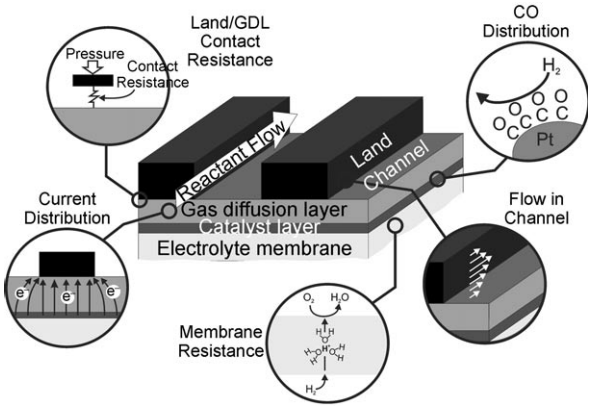

Figure 1. Illustration of the range of in situ diagnostics techniques applied by the authors to PEFCs.

used that incorporated an array of discrete current collection points, which allowed localised electrical measurements to be performed across the lateral extent of the fuel cell. Figure 2 illustrates the experimental approach adopted. Electrical measurements (current density, contact resistance, localised voltammetry and electrochemical impedance) are made using an array of contacts fabricated using printed circuit board (PCB) technology, similar to that of Cleghorn et al.,[19] although the electronic configuration we used was more sophisticated. Each contact is associated with its own load circuit which allows electrical measurements to be made at each of the discrete locations on the board.

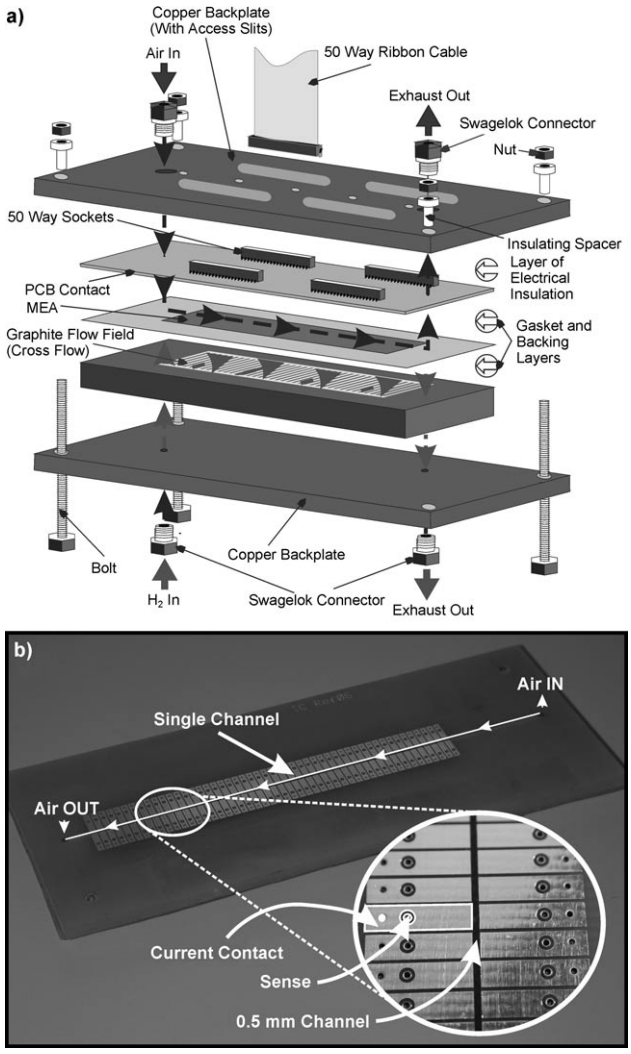

Figure 2. Experimental apparatus used to perform in situ measurements. a) Exploded view of a single-channel fuel cell; b) printed circuit board with individual current contacts.

A single linear channel flow-field was investigated for the localised electrical measurements in this study. The reasons for this are:

- Once understanding of the processes occurring in a single channel is established, it is possible to extend that knowledge and apply it to an entire flow-field; it is impossible to start from the flow-field and determine anything about the effect of individual channels.
- From a computational viewpoint, simulation of a single channel is much simpler than a full flow-field, therefore facilitating model validation.
- Starting from a single channel provides the basis from which the effect of introducing extra features (i.e. corners, parallel channels, internal channel modifications such as wall texturing or baffles) can be judged.
- The relationship between the channel and the GDL can be better understood from the study of a single channel. The lateral transport of reactant away from the channel within the GDL is much less complicated to measure for a single linear channel. This is illustrated particularly well in studies of CO distribution mapping, as described later.

Full details of the experimental approach are given in the references to each section below, including both PEFC and SOFC techniques.

4. Polymer Electrolyte Fuel Cell Diagnostics

4.1. Contact-Resistance Distribution

The way in which a fuel cell or stack is put into compression has a significant effect on the performance of the system. Poor contact between the current collection plate and the electrode results in a high contact resistance, and this may vary across the extent of the cell. Figure 3 shows the contact-resistance distribution across the single-channel fuel cell under three different clamping regimes.[87] It can be seen how different clamping pressures applied to the tie-rods shown in Figure 2a affect the contact resistance (i.e. a nominally even compression force produced by a torque of 8 Nm to each bolt, at 6 Nm to each bolt and a gradient of torque running 8–5–3 Nm from left to right). It should be noted that it is difficult to predict what effect a certain tie-rod torque will have on the contact resistance distribution. It was qualitatively noted that the order and the increment in which the bolts are tightened has a major effect on the contact-resistance distribution. For example, increasing the clamping force at one end of a cell will

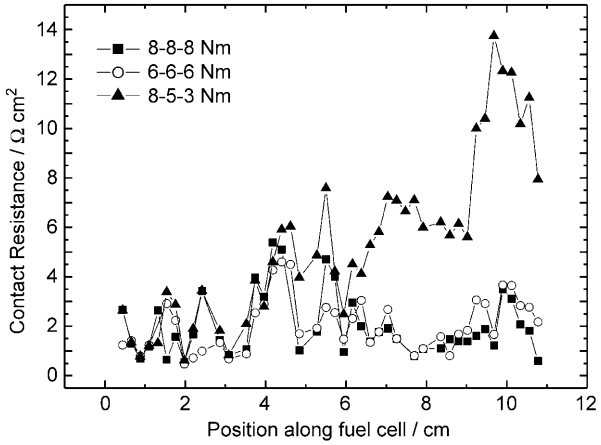

Figure 3. Contact-resistance distribution along the length of a PEFC for three different clamping modes.[87]

affect the contact resistance at the other end to a certain extent, as well as at the end of the tightening. The bolts should be tightened in a balanced order, with bolts diametrically opposed tightened consecutively, as is the case for most flanged bodies.

4.2. Current Distribution

Figure 4 shows the current-density profile as a function of position along the fuel cell channel at three different operating potentials, including the potential-versus-current (polarisation) plots for a selection of contacts at different points along the channel.[33] It can be seen that increasing the electrical load leads to a more heterogeneous distribution of current density, with heavy electrical loading (0.3 V) showing a rapid drop in current density along the channel due to the consumption of reactant 'upstream'. This results in the latter half of the channel being starved of oxygen.

The inset to Figure 4 is a graph of polarisation versus current density as a function of position along the channel. Inspection of these polarisation plots illustrates the 'reactant starvation' effect further. The form of the polarisation plots may seem counter intuitive upon first inspection, in that for points further along the channel, the *I–V* curves 'fold-back' onto themselves at lower potentials. This may be understood by appreciating that at lower potentials the contacts closer to the input of the channel will utilise more of the available reactant. This will deprive the subsequent (downstream) contacts of reactant to an increasing extent along the channel. The overall cell-polarisation characteristic displays a conventional mass-transport-limited upper current limit, at the start of the channel there is no sign of reactant starvation; however, towards the end of the channel we see a rapid loss of current density due to consumption of reactants further upstream. The upstream consumption of reactant starves the downstream portion of the channel, such that increasing the load on the cell leads to greater current generation at the start of the channel and a reduction in current at the end; this leads to a 'current inversion' phenomenon.

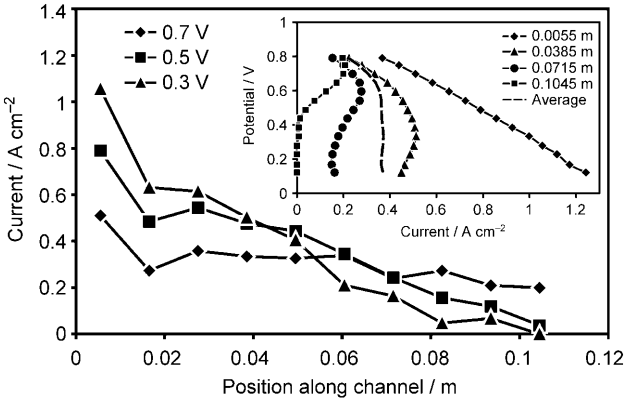

Figure 4. Current-density distribution along a single-channel fuel cell with air supplied to the single channel at different polarisations.[33]

These current-mapping measurements have validated the results of a comprehensive numerical model of fuel cell operation[88] and have shown that provided the electrolyte membrane does not suffer from dehydration, a simple analytical expression can be used to describe single-channel fuel cell performance over a wide range of operating conditions.[89]

Effect of Flow-Channel Width on Current Distribution

Flow-field design and the materials of construction have a significant effect on fuel cell performance due to factors such as reactant distribution, water management, back-pressure and Ohmic resistance.[90] Advanced methods of numerical simulation have gone some way to predict the consequences of adopting a particular flow pattern or feature size[91–93] and some experimental work has been performed to examine the effect of channel and land geometry on performance.[94,95] The single-channel geometry used here allows the channel width to be examined in isolation from a full flow plate.

Figure 5 shows the bulk cell-polarisation response for a range of channel widths. The shape of the polarisation response is of the conventional form, with each profile exhibiting a linear slope in the Ohmic-resistance-dominated region (the gradient of which is approximately constant for each channel width), and the mass-transport limiting current increasing with the air flow rate.[87]

Figure 6 compares the total current and the oxygen utilisation at three potentials for each channel width. At low flow rates there is minimal difference between the total current for any of the channel widths, this is due to the complete utilisation of the oxygen. Overall the current generated and the amount of oxygen utilised for each channel width tends to increase in the order $0.5 < 3 < 1 < 2$ mm. In general, the channel widths of 1 and 2 mm exhibited a similar response and performed better than widths of 0.5 and 3 mm. The difference between each channel is most discernible under conditions of high flow rate and low cell potential (high electric loading); although even at 0.7 V, under higher air flow rates, the performance of the 1 and 2 mm channels is about 50% greater than that for the 0.5 and 3 mm channels. The significant reduction in performance of the 3 mm channel is surprising. It is clear

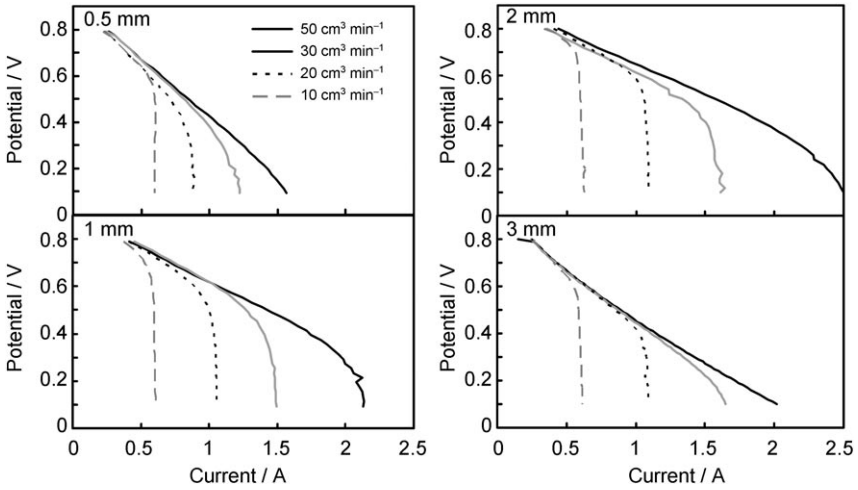

Figure 5. Polarisation plots for different channel widths with varying air flow rate.[87]

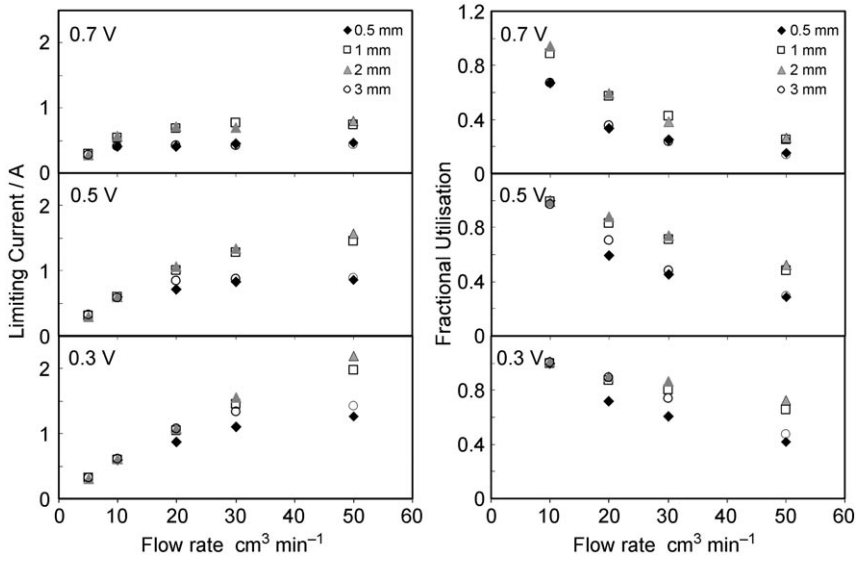

Figure 6. Limiting current and fractional utilisation for different channel widths with varying air flow rate and operating voltages.[87]

changing the channel width will be due to the resistance of the GDL and not the contact resistance. So increasing the channel width (with effectively no change in the land contact area), increases the Ohmic losses of the system. As a consequence, increasing the channel width, despite directly exposing more of the reactant to the catalyst, will start to have a detrimental effect on performance due to increased Ohmic losses.

To demonstrate this point further, the channel area specific resistance (ASR) for each channel width is compared in Figure 7. It can be seen that the ASR increases with channel width, as would be expected, due to the increased current path distance. However, when the channel width is accounted for by dividing the ASR by the channel width, the channel length specific resistance (a measure of the performance of each channel regardless of its width), shows that a channel width in the region of 1–2 mm results in the lowest resistance. This is also in accord with the relative performance of each channel based on the limiting current (i.e. $2 > 1 > 3 >$ 0.5 mm) and modelling studies described at the start of this section.

that making the channel too wide imposes a large lateral Ohmic drop and also impairs the performance of the fuel cell.

Two of the main factors in determining the impact on cell efficiency of a given channel width are the effect it has on the internal resistance of the cell and the extent to which the reactant is exposed to the catalyst; however, water management will also have an influence. It has been reported that decreasing the land width to less than a certain value leads to a performance decrease due to increased Ohmic losses, despite increasing the open channel density.[95] In the single-channel setup used in this investigation, the size of the land remains effectively constant relative to the width of the channel. As such, there will be no significant increase in the Ohmic losses of the fuel cell caused by decreasing the land area. In addition, the contact resistance between the current collecting electrode and the GDL is compensated for by the electronic load. Therefore, any increase in the Ohmic loss of the fuel cell caused by

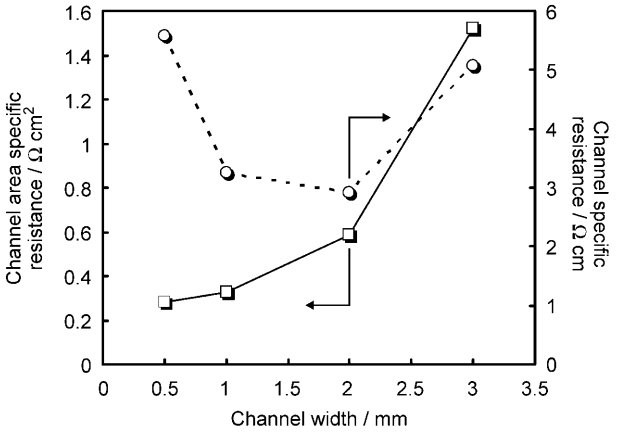

Figure 7. Channel area specific resistance and channel specific resistance with channel width.[87]

4.4. Localised Impedance Spectroscopy

Figure 8a shows the current distribution along the length of the cathode flow channel at a high (0.6 V) and low (0.8 V) electrical loading.[49] The behaviour at high loading has been described above and is attributed to a reactant-starvation effect. Figures 8b,c show the complex plane plots at different positions along the channel. It is immediately clear that the EIS response contains much more information than the dc measurements. At 0.8 V (Figure 8b), a clear trend is observed as the arc radius increases with distance along the channel. The dc response shows no significant sign of a decrease in current density along the channel so the reaction is not being limited by reactant consumption. However, as the reactant is being consumed along the channel, so there will be a depletion of oxygen in the channel and diffuser. The EIS plot at 0.6 V (Figure 8c) shows that for positions towards the end of the channel, a distinct direction change is observed, away from the closing of the semicircle. This means that a situation exists in which an increase in reactant consumption, with a corresponding current increase, at one point in the fuel cell (brought about by a decrease in cell voltage) can cause a *decrease* in current at another point of the fuel cell. The impedance feature seen here is a manifestation of operation under conditions of reactant starvation leading to a negative differential resistance in the polarisation plot, as seen in the inset in Figure 4.[49]

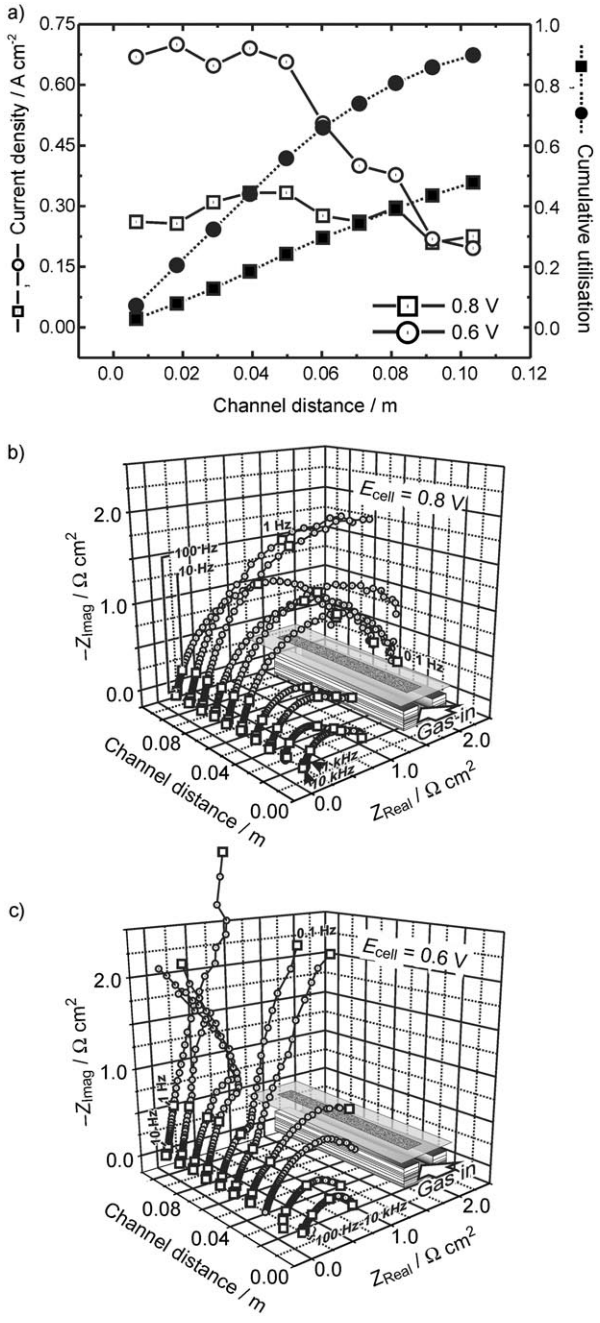

Figure 8. a) Current-density distribution and oxygen utilisation at 0.8 and 0.6 V; b) complex plane EIS plots as a function of distance along the channel at cell potentials 0.8 V and c) at 0.6 V.[49] Reproduced by permission of The Electrochemical Society.

Figure 9 compares the localised impedance response at the start and end of the channel with that of the bulk impedance response for operation at 0.6 and 0.8 V.[49] At 0.8 V, although the form of the bulk response has the same shape as that at the beginning and end of the channel, the size of the arc varies considerably. At 0.6 V, the form of the bulk response is significantly different to that at the beginning and end of the channel. These results show how conventional impedance measurements on the bulk fuel cell would not be representative of how the system is actually performing, especially under low stoichiometry conditions, and could actually be misleading if spatially homogeneous operation is assumed to be occurring.

4.5. Electrolyte-Resistance Distribution

By following the procedure described in the last section for the localised impedance measurements, but by concentrating on the point at which the impedance response crosses the real axis at high frequency, it is possible to measure the internal Ohmic resistance of the system; this is predominantly due to the resistance of the electrolyte and thus the level of hydration.

A complete description of current and electrolyte-resistance distributions has been given over a range of electronic load, temperature and humidification conditions as well as an analysis of the complex interaction of current and membrane humidification.[96] The results show that for the majority of operating modes, the analytical approach developed by Kulikovsky and Kornyshev to describe current-density distribution, provides accurate results.[89] However, under certain conditions where the membrane becomes significantly dehydrated, leading to high electrolyte resistance, the model cannot account for this behaviour. For example, Figure 10 shows the variation in current density and membrane resistance for a cell with high air flow rate operating over a range of temperatures. The effect of membrane dehydration at the start of the channel can be seen to increase with temperature as the air stream, which is under humidified extracts water from the membrane at the start of the channel. As a consequence, the current is seen to *increase* along the length of the channel. The analytical

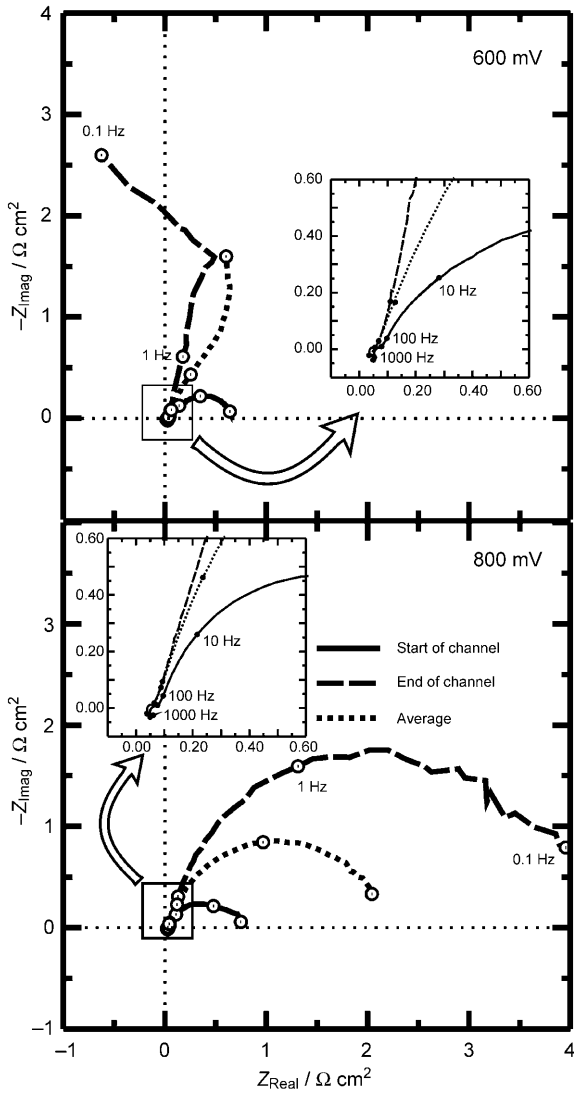

Figure 9. Comparison of the localised EIS response at the start and end of the channel with the bulk response at 0.6 and 0.8 V.[49]

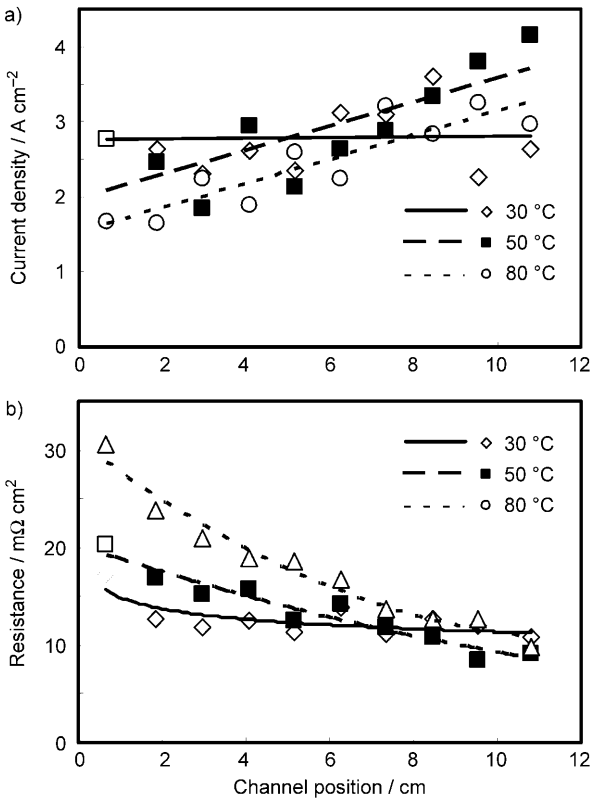

Figure 10. a) Current distribution and b) membrane-resistance distribution of a single-channel fuel cell operating at high air flow rate showing the effect of membrane dehydration at the start of the channel, the effect of which increases with temperature.[96]

model does not account for this phenomenon and therefore cannot capture the effect.

4.6. Carbon Monoxide Distribution

PEFCs are highly sensitive to carbon monoxide in the hydrogen feed stream, since it poisons the Pt in the anode. Whilst extensive studies have been made of the mechanism of CO poisoning, little attention has been paid to the spatial distribution of this poisoning process across the extent of the anode. Assuming that the fuel cell is physically homogeneous, that is, the catalyst is evenly dispersed, the GDL is of even thickness, porosity and composition and the fuel cell is isothermal, three factors will determine where CO poisoning is located. These are the convective transport component along the channel, diffusion within the GDL (driven by a concentration gradient) and the local level of CO coverage of the catalyst.

To study the distribution of CO in a fuel cell, an approach was adopted in which pulses of CO are injected into the single-channel cell, local current associated with the adsorption is measured and then the CO is electrochemically stripped from the surface in order to obtain the local concentration of CO on the surface.[97] With a knowledge of the roughness factor of the platinum catalyst layer, it is possible to use the localised CO stripping charge to develop a map of where it is adsorbed. Figure 11 shows the CO distribution with varying carrier-gas flow rates. Such a map may be very useful in understanding the pattern of poisoning within an operating fuel cell or in understanding the balance between reactant convection and diffusion in an operating fuel cell. Results from this set of experiments have been used to support the development of a numerical model of CO distribution which has allowed the effect of reformer 'burping' and start-up conditions to be simulated.[98]

Channel-Flow Mapping

To validate the technique of LDA as applied to fuel cells, the behaviour of reactant flows within the air-side flow channel at a 180° U-turn (or switchback) of a working PEFC has been studied.[87] LDA is a non-invasive optical technique used to measure the velocity of tracer particles moving in a fluid flow.[99] A beam from a laser source is passed through a beam

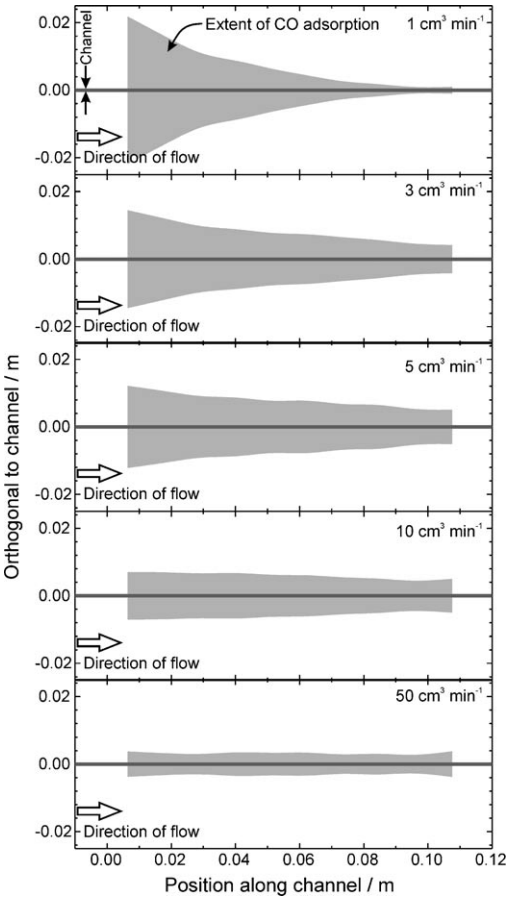

Figure 11. Measured CO distribution along the single channel of the fuel cell with varying carrier-gas flow rate and a constant CO injection amount of 0.2 cm^3.[97]

splitter and the two resultant coherent laser beams, one of which is frequency-shifted using a Bragg cell, are focused onto a measurement point where the beams intersect, as shown in Figure 12. Figure 13 shows the optical fuel cell built of Perspex and composed of a single "switchback" flow-field, the laser beams can be seen focused into the flow channel of the cell.

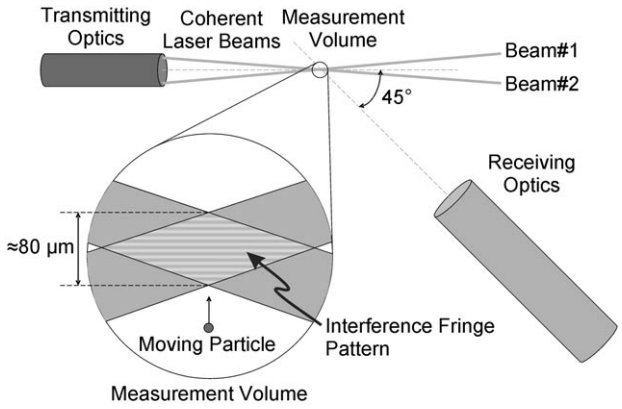

Figure 12. Formation of the measurement volume and the orientation of the optics in an LDA experiment.

Figure 13. Optical PEFC with two laser beams focused to a point within the flow channel.

In this measurement region, an interference pattern is produced, creating a series of bright and dark fringes, which moves due to the frequency shift between the beams. As a particle suspended in the flow of interest moves through this sequence of fringes, light is scattered in all directions, the intensity of which is determined by the size of the particle, its refractive index and the position of the observer. The scattered light is observed using a receiver lens which focuses light onto a photomultiplier, converting the incident light intensity into an electrical signal (the Doppler burst). The frequency of the Doppler burst is dependent upon the distance between interference fringes and the velocity of the tracer particle, and is determined by fast Fourier transform processing using a signal analyser. Since the fringe spacing can be determined using properties of the laser beams, such as wavelength of light and beam geometry, it is possible to infer the velocity of the tracer particle normal to the fringe planes. Also, since the fringe pattern is moving it is possible to measure zero velocities of stationary particles.

Figure 14 shows profiles of velocity components parallel to the MEA surface. The velocity vectors are shown scaled relative to the mean flow velocity in the channels. The velocity profile indicated at point *A* is representative of a typical flow over a porous surface,[100] with a no-slip condition at the Perspex surface and a slip velocity at the porous interface. This behaviour is clearly not consistent with the general flow around the corner, as significant variation in the measured velocity profiles can be seen.

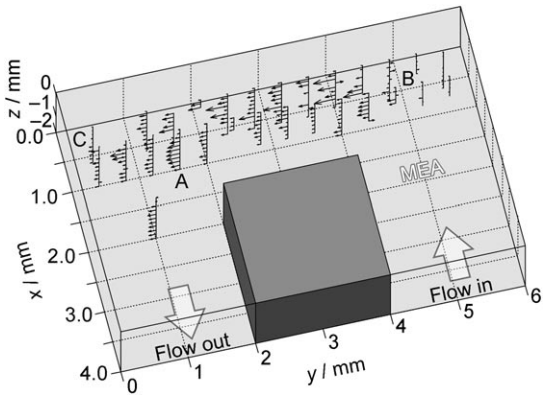

Figure 14. Velocity profiles a the "switchback" of a flow channel for a PEFC operated at a current density of 0.1 A cm^{-2}.[87]

Around the region indicated at point *B*, the measured velocities are small in magnitude and varying in direction, indicating the presence of a stagnant region with some recirculation. This has also been observed by Martin et al. in a system of identical geometrical shape but different scale.[101] The presence of the stagnant region reduces the cross-sectional flow area, accelerating the flow. A recirculation area can also be seen in the region of *C*; however, it is much smaller than at *B*.

A description of the full range of features observed is beyond the scope of this Minireview; however, it can be summarised by stating that the expected secondary flow features are present, but additional complexity is also manifest due to a combination of the operating MEA and the flow disturbance caused by the abrupt change of wall direction. The implication of the findings is that the assumption of uniform composition immediately above the MEA cannot be assumed and the flux of species to/from the MEA must vary in regions where severe flow deflection exists. This can be expected to produce problems for fuel cells being driven at high current loadings.

5. Solid Oxide Fuel Cell Diagnostics

5.1. Temperature Mapping

The high-temperature operation of SOFCs (500–1000 °C) makes the application of many of the techniques described for the PEFC much more difficult. However, it is the high temperature of operation and the sensitivity of ceramic structure to thermal gradients that makes the study of temperature distribution in SOFCs of particular interest.

Using pellet SOFCs and thermal imaging camera technology, temperature maps of the cathode during electrical loading have been achieved.[102] Figure 15 shows the change in temperature associated with changing the load on the cell. Using this system, a temperature and spatial resolution of <0.1 °C and <1 mm could be achieved with a frame capture rate of 100 Hz, allowing rapid transients to be captured. In combination with modelling studies, these measurements have allowed phenomena such as the self-heating effect on polarisation response to be accounted for.[102]

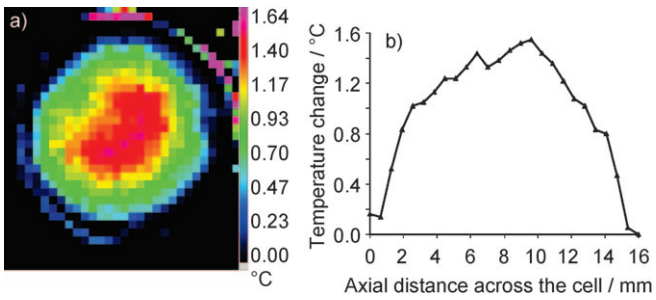

Figure 15. Temperature change during a polarisation curve measurement at 592 °C: a) temperature difference between open circuit and 0.2 V; b) profile of this temperature difference across the cell.[102]

5.2. Thermal-Stress Analysis

Given that ceramic materials are brittle and have inherent flaws randomly distributed throughout their volume, there are two main factors which determine if ceramic structural components will fail in service: the level of stress which the component experiences and the distribution and size of the pre-existing flaws. Considering the first factor, because of the high temperature of operation the mechanism by which some of the largest stresses are generated in an SOFC is that of thermal expansion. Uniform thermal expansion in itself does not generate stress, instead it is the result of variations in temperature across components, or some form of mechanical constraint (such as perimeter seals or friction between the interconnects and cell structure) that prevents the material from expanding freely. Therefore, the magnitude of thermally induced stresses in an operating fuel cell will depend on any temperature gradients present, the properties of the materials and the degree of constraint that the components experience. Figure 16 shows

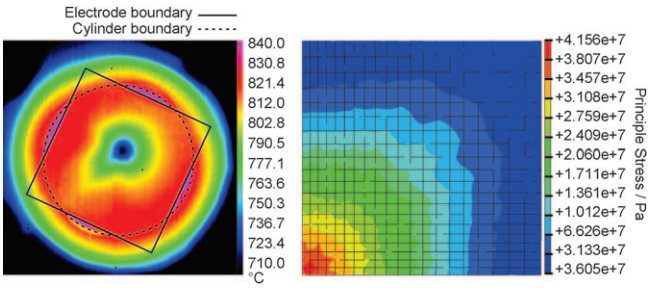

Figure 16. Left: Infrared image of an electrolyte-supported SOFC while 6 $dm^3 min^{-1}$ of nitrogen is blown at the centre of the anode; furnace temperature: 829 °C. The square indicates the electrode area and the circle shows the glass tube onto which the sample is mounted. Right: Minimum principal stress field across the anode outer surface.[103] Reproduced by permission of The Electrochemical Society.

an example of the kind of temperature distribution, measured using the thermal camera technique, induced across the surface of an electrolyte supported SOFC (40 mm × 40 mm) held at operating temperature (829 °C) while a stream of 'cold' nitrogen is directed at the middle of it to induce a thermal (and stress) gradient.[103]

At high nitrogen flow rates, local cooling at the centre of the cell by as much as 100 °C (thermal gradients of up to 9 °C mm^{-1}) could be applied repeatedly and rapidly, without delamination or cracking of the sample. Using the temperature map as an input to a thermal-stress model, the stress distribution in the cell can be calculated as shown in Figure 16.[103]

5.3. Reference Electrodes for SOFCs

The ability to deconvolute the performance of the anode, cathode and electrolyte resistances is one of the most fundamental requirements for fuel cell diagnostics. To do this, it is necessary to accurately determine the polarisation behaviour of each electrode independently. This can be achieved by using a refer-

ence or third electrode. Three-electrode techniques are commonly used in aqueous electrochemistry, where a current is passed through the working and counter electrode and changes in potential are recorded relative to a reference electrode, the potential of which remains constant as current is passed. Various reference-electrode approaches have been applied for the PEFC, as reviewed by Hinds.[104] However, the application of three-electrode techniques in SOFC electrochemistry is problematic due to the relatively high electrolyte resistance compared to aqueous systems, and the fact that the reference electrode cannot be easily incorporated into the electrolyte and must instead be placed on an external electrolyte surface. Under these conditions, incorrect use of a reference electrode can readily lead to inaccurate and misleading results. In addition, a true reference electrode requires a stable environment that typically involves a redox couple at equilibrium; the geometry of the electrolyte pellet, position and registry of the anode, cathode and reference electrode are all very important.

The authors have developed an experimental procedure and correction method to take into account the current dependence of the series resistance between the region of electrolyte experienced by the reference electrode under load and the working electrode. The procedure can be applied to geometries with non-uniform current densities where the relative potential of the region of electrolyte in contact with the reference electrode is changing when current is drawn. It is shown that it is possible to extract information on the electrochemical processes occurring by changing reaction conditions and investigating the effect upon the exchange current density.[105]

5.4. In situ Raman Spectroscopy

Raman spectroscopy is a material-specific analytical technique which offers sample-identification capabilities down to micron spatial resolutions. It is extremely flexible as any excitation wavelength may be used, unlike fluorescence; it is also non-invasive. The application of Raman to the study of SOFCs is limited and has only been used relatively recently for the study of SOFCs under practical operating conditions, and even then only for high-temperature SOFCs based on yttria-stabilised zirconia (YSZ) electrolyte.[106,107] In our labs, the authors have shown that Raman spectroscopy can be used as a probe of electrolyte surface temperature and electrolyte stoichiometry, with work currently looking at Ni/NiO redox processes, sulphur formation on the anode of SOFCs and coke formation, as described by Pomfret et al.[108]

5.5. Electrolyte Temperature

Raman spectroscopy is particularly sensitive to the temperature of the sample volume probed. Both peak position and width are affected by changes in temperature, due to the anharmonic nature of vibrational modes. As a result, the precise peak position or width may be used to estimate the temperature of the surface. Figure 17 shows the Raman spectra of YSZ and gadolinium-doped ceria (CGO) electrolytes taken using a

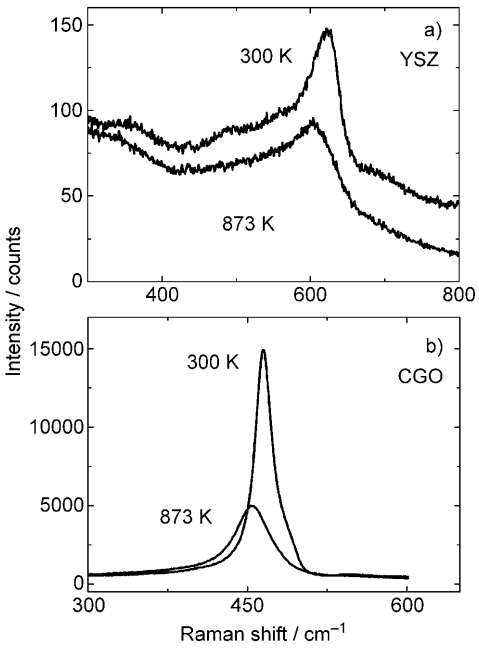

Figure 17. Raman spectra of a) YSZ and b) CGO taken using the 633 nm laser at full power and a 10 s integration taken at 300 and 873 K. Note the large difference in intensity between the two spectra and the difference in the spectral range.[109]

633 nm laser. The Raman cross-section of YSZ is clearly much smaller than that of CGO. The spectral feature of YSZ is also quite broad making the extraction of temperature information more difficult.[109]

The spectrum of the CGO sample in contrast is dominated by a well-defined, intense Raman peak centred at approximately 460 cm^{-1}. By using the position on this mode, it was possible to use it as a diagnostic of temperature with a spatial and temperature resolution of 1 μm and 2.5 °C, respectively, although superior Raman instrumentation could improve on the temperature resolution by an order of magnitude. These results pave the way for the development of an in situ technique capable of mapping temperature distribution at very high spatial resolution in operational SOFCs. Such a facility will be particularly useful for studying very structured and defined electrodes for work on electrode kinetic measurements.

Electrolyte Stoichiometry

Raman spectroscopy has also been investigated as a probe of the oxidation state of CGO electrolyte. The non-stoichiometry of ceria has been studied extensively and has been found to be a function of the dopant, temperature, and gas composition.[110] Ceria can be reduced in the presence of H_2 to give a number of non-stoichiometric forms of CeO_{2-x}, where $1.7 \leq 2-x \leq 2$.[111] The inset of the top panel of Figure 18 shows the predicted oxidation state of ceria at 873 K as a function of pH_2 and pH_2O. Although the presence of gadolinium dopant is likely to affect the exact phase properties, the thermodynamic analysis shows that we might expect there to be three possible phases within the realm of the operating conditions imposed

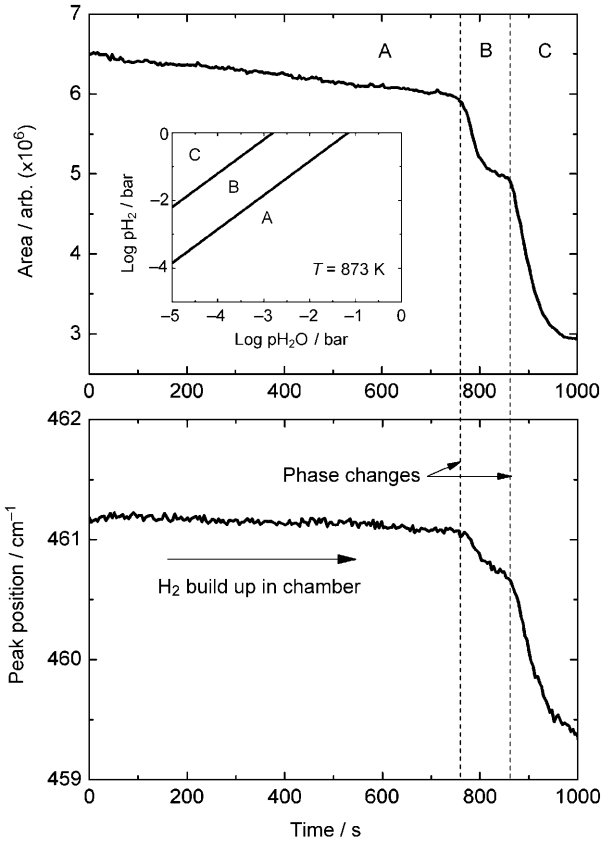

Figure 18. Peak area (top) and position (bottom) of the 460 cm^{-1} mode of CGO as a function of time after beginning to flush the stage with 100% H_2 gas at 873 K. Top (inset): predicted oxidation state of ceria at 873 K as a function pH_2 and pH_2O.[109]

on the system, those being: A) CeO_2, B) $CeO_{1.85}$ and C) $CeO_{1.72}$. These results suggest that it may be possible to map the oxidation state of CGO within an operational fuel cell when under load.

5.6. Mapping Electrode Microstructure

Thus far, this Minireview has concentrated on functional mapping of the various physical processes occurring in fuel cells. In this final section, attention is turned to mapping the physical distribution of electrode materials; effectively creating 3D microstructural maps of fuel cell electrodes.

SOFC electrodes are commonly composite materials, which provide intimate contact of the electronic, ionic and pore phases at triple phase boundaries (TPB).[112] The length and distribution of these TPBs is widely thought to influence the electrochemical performance of the cell, and as such these can be thought of as electrochemically active zones. Furthermore, electrode microstructure is known to affect the Ohmic, diffusion and mechanical properties of the cell.

However, the link between electrode microstructure and performance is traditionally poorly understood. Whilst attempts have been made to optimize electrode microstructures empirically, the large number of processing and environmental conditions affecting microstructure makes this practically difficult. Furthermore, the inherent limitations of studying complex microstructures in 2D limit the experimenter's ability to quantify microstructural changes by conventional microscopy.

Recent advances in tomography procedures have provided access to 3D microstructural data at unprecedented level of resolution. Wilson et al.[113] were the first to report 3D reconstruction of an SOFC electrode: using a focused ion beam (FIB) technique, the electrode structure can be sequentially milled and imaged to obtain a sequence of 2D images that can be effectively recombined in 3D space. Subsequently, FIB tomography has been more widely adopted for geometrical and modelling studies of a variety of SOFC anode[114–118] and cathode materials.[119–122]

The resolution of conventional X-ray computed tomography (CT) has traditionally limited its application to the study of electrode microstructures. The development and implementation of X-ray optics has led to a near order-of-magnitude improvement in spatial resolution obtainable, allowing application in the study of the characteristically sub-micron features of SOFC electrodes.

In 2008, Izzo et al. demonstrated the use of X-ray nano-CT for the study of pore distribution in composite electrodes, subsequently applying a lattice-Boltzmann type simulation to the experimentally derived microstructures.[123] A review of advanced microstructural characterisation techniques provides further insight into the developments and application of tomography procedures.[124]

The authors have developed methodologies for 3D imaging of SOFC electrodes using both FIB and nano-CT techniques, recognising the benefits of these complementary techniques for correlative studies of electrode microstructures. Alongside experimental characterization tools, a suite of numerical techniques have been developed for simulation and interpretation of experimentally derived microstructures and numerically generated microstructural analogues.

Golbert et al. developed a platform for generating microstructural analogues of SOFC electrodes; using Monte Carlo modelling techniques, spheres of three materials (corresponding to the electronic, ionic and pore phases) are distributed in 3D with a probability weighted to the expected volume fraction of the final electrode structure.[125] A numerical expansion of the solid phases is subsequently performed to simulate the sintering step. A number of geometrical parameters can be derived from the resulting microstructure which has also been used as the basis for an electrochemical simulation. These geometrical analysis tools have also been successfully applied to electrode microstructures derived from FIB and X-ray tomography experiments.[126–130]

Shearing et al. have utilised FIB-derived tomography data as the framework for an electrode simulation using the active TPB lengths to serve as electrochemically active sites for current generation according to the Butler–Volmer equation.[126] The simulation originally developed for use with Monte Carlo-type numerically generated structures has been successfully integrated with the Ni-YSZ tomogram. The experimentally derived microstructure (see Figure 19a) enables accurate prediction of

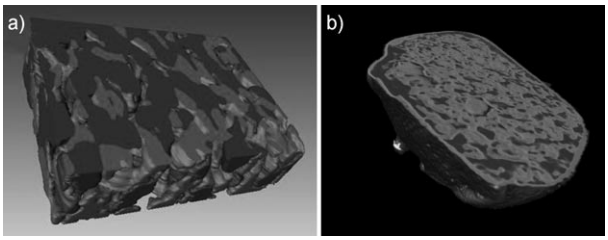

Figure 19. a) A reconstruction of a Ni-YSZ electrode microstructure obtained using serial-sectioning FIB tomography. Light grey corresponds to the YSZ phase, dark grey to Ni and pore space is void. The total sample volume is $6.68 \times 5.04 \times 1.50$ μm.[126] b) A reconstruction of Ni-YSZ electrode microstructure using X-ray nano-CT, the 3D volume rendering showing changes in X-ray absorption corresponding to composition differences in the composite microstructure (total volume of reconstruction: 37945 μm^3).[127]

current density and the transport of gas and charged species within the structural constraints of the real system. By adopting an iterative approach to match experimental and simulated results, the exchange current per unit triple-phase boundary is also extracted.

The complementary use of X-ray and FIB tomography has enabled direct comparison of the two techniques, which has shown good agreement for solid-pore phase volume analysis of an SOFC electrode.[127] Using the techniques in parallel, material volumes spanning more than two orders of magnitude were characterized, demonstrating the advantages of both approaches to balance the dual requirements of resolution and analysis volume for different materials.

In lab-based systems, characteristic changes in X-ray absorption have been identified, whilst these have not been sufficiently uniform to facilitate segmentation of the solid phases in composite electrodes, they signal the potential to isolate material phases using synchrotron radiation. Figure 19b shows an example of the spatial distribution of X-ray attenuation for a Ni-YSZ electrode.

Using synchrotron radiation it is possible to tune the X-ray energy of the source with great accuracy, allowing the selection of a narrow band-width of X-ray energies, which can be optimized for the specific material(s) under investigation. The photon energy can then be manipulated about the X-ray absorption edge of one material to provide elemental and chemical state identification.

XANES (X-ray absorption near-edge spectroscopy) takes advantage of the discontinuity in X-ray absorption across a range of photon energies. At photon energies just above the binding energy of an electron in an inner orbit, photoelectric absorption is more likely to occur than at photon energies just below the binding energy. This photon energy corresponds to the absorption "edge" which describes this discontinuity in the attenuation behaviour of a given material. Characteristic changes induced at energies above and below an 'edge' allow phase identification.

With increasing maturity, the applications of high-resolution tomography provide an opportunity to explore a range of material systems under different operating and processing conditions. Because of their non-destructive nature, X-ray techniques are particularly attractive for characterisation of dynamic microstructural change because of their non-destructive nature.

Tomography applications are not restricted to study of SOFC electrodes and work is underway to apply these techniques to PEFC microstructures and other electrochemical devices.

6. Summary and Outlook

This Minireview has discussed the range of diagnostic techniques reported in the literature for the study of the internal workings of fuel cells and focused on work performed by the authors to build a map of how fuel cells work at both the device and microstructural level. In situ diagnostic techniques continue to reveal more about the working of fuel cells and in so doing allow for improved cell hardware design, materials selection and choice of operating conditions to realise advanced electrochemical performance and longevity. These techniques also allow us to scrutinise the validity of conventional bulk electrical measurements and develop detailed models of fuel cell operation.

There is increasing demand for reliable diagnostic techniques from developers of fuel cell hardware and models. The use of these techniques applied to cells is quite mature and the range of approaches has proved very useful. Many of the techniques developed for scientific understanding may also be applicable as practical on-board sensors for monitoring and control. However, more examples of mapping techniques applied at the stack level and micro-scale are still required. Mapping the processes occurring within electrodes is particularly important for understanding the mechanisms of degradation and failure; the authors predict that there will be significant developments in this field.

Acknowledgements

The authors would like to acknowledge the EPSRC for funding the work on current mapping through grant: GR/M 73552 and through grant EP/G060991/1 along with the NPL for support of Dr. Kalyvas. The EPSRC Supergen Fuel Cell programme (Phase 1) is acknowledged for funding the thermal imaging research and Phase 2 for the electrode microstructure mapping work. We thank Johnson Matthey for supplying bespoke MEAs and to Intelligent Energy for their support of our current work. Dr. Ladewig acknowledges financial support from the British Council and Dr. Maher for support from the King Abdullah University of Science and Technology (KAUST) for supporting the Raman spectroscopy research. We acknowledge Mr. S. Turner for technical assistance in the design and construction of the current mapping fuel cell hardware and Mr. R. Rudkin for his unparalleled practical knowledge of SOFCs.

Keywords: fuel cells · imaging · instrumentation · mapping · metrology

[1] W. K. Lee, C. H. Ho, J. W. Van Zee, M. Murthy, *J. Power Sources* **1999**, *84*, 45 – 51.
[2] Ch. Wieser, A. Helmbold, E. Gülzow, *J. Appl. Electrochem.* **2000**, *30*, 803 – 807.
[3] S. Slade, S. A. Campbell, T. R. Ralph, F. C. Walsh, *J. Electrochem. Soc.* **2002**, *149*, A1556 – A1564.
[4] S. Miachon, P. Aldebert, *J. Power Sources* **1995**, *56*, 31 – 36.
[5] J. Ihonen, F. Jaouen, G. Lindbergh, G. Sundholm, *Electrochim. Acta* **2001**, *46*, 2899 – 2911.
[6] R. C. Makkus, A. H. H. Janssen, F. A. de Bruijn, R. K. A. M. Mallant, *J. Power Sources* **2000**, *86*, 274 – 282.
[7] D. P. Davies, P. L. Adcock, M. Turpin, S. J. Rowen, *J. Appl. Electrochem.* **2000**, *30*, 101 – 105.
[8] D. P. Davies, P. L. Adcock, M. Turpin, S. J. Rowen, *J. Power Sources* **2000**, *86*, 237 – 242.
[9] C. Lim, C. Y. Wang, *J. Power Sources* **2003**, *113*, 145 – 150.
[10] L. R. Jordan, A. K. Shukla, T. Behrsing, N. R. Avery, B. C. Muddle, M. Forsyth, *J. Appl. Electrochem.* **2000**, *30*, 641 – 646.
[11] L. R. Jordan, A. K. Shukla, T. Behrsing, N. R. Avery, B. C. Muddle, M. Forsyth, *J. Power Sources* **2000**, *86*, 250 – 254.
[12] E. Passalacqua, G. Squadrito, F. Lufrano, A. Patti, L. Giorgi, *J. Appl. Electrochem.* **2001**, *31*, 449 – 454.
[13] P. L. Hentall, J. B. Lakeman, G. O. Mepsted, P. L. Adcock, J. M. Moore, *J. Power Sources* **1999**, *80*, 235 – 241.
[14] D. Natarajan, T. V. Nguyen, *J. Electrochem. Soc.* **2001**, *148*, A1324 – A1335.
[15] R. Eckl, R. Grinzinger, W. Lehnert, *J. Power Sources* **2006**, *154*, 171 – 179.
[16] P. C. Rieke, N. E. Vanderborgh, *J. Electrochem. Soc.* **1987**, *134*, 1099 – 1104.
[17] J. J. T. T. Vermeijlen, L. J. J. Janssen, *J. Appl. Electrochem.* **1993**, *23*, 26 – 31.
[18] J. Stumper, S. A. Campbell, D. P. Wilkinson, M. C. Johnson, M. Davis, *Electrochim. Acta* **1998**, *43*, 3773 – 3783.
[19] S. J. C. Cleghorn, C. R. Derouin, M. S. Wilson, S. Gottesfeld, *J. Power Sources* **1998**, *28*, 663 – 672.
[20] C. Wieser, A. Helmbold, E. Gulzow, *J. Appl. Electrochem.* **2000**, *30*, 803 – 807.
[21] Y. G. Yoon, W. Y. Lee, H. Yang, G. G. Park, C. S. Kim, *J. Power Sources* **2003**, *118*, 193 – 199.
[22] M. Noponen, T. Mennola, M. Mikkola, T. Hottinen, P. Lund, *J. Power Sources* **2002**, *106*, 304 – 312.
[23] M. Noponen, T. Hottinen, T. Mennola, M. Mikkola, P. Lund, *J. Appl. Electrochem.* **2002**, *32*, 1081 – 1089.
[24] T. Hottinen, M. Noponen, T. Mennola, O. Himanen, M. Mikkola, P. Lund, *J. Appl. Electrochem.* **2003**, *33*, 265 – 271.
[25] M. Noponen, J. Ihonen, A. Lundblad, G. Lindbergh, *J. Appl. Electrochem.* **2004**, *34*, 255 – 262.
[26] M. M. Mench, C. Y. H. Wang, *J. Electrochem. Soc.* **2003**, *150*, A79 A85.
[27] M. M. Mench, C. Y. Wang, M. Ishikawa, *J. Electrochem. Soc.* **2003**, *150*, A1052 – A1059.
[28] H. Sun, G. S. Zhang, L. J. Guo, H. T. Liu, *J. Power Sources* **2006**, *158*, 326 – 332.
[29] A. Hakenjos, H. Muenter, U. Wittstadt, C. Hebling, *J. Power Sources* **2004**, *131*, 213 – 216.
[30] S. A. Freunberger, M. Reum, J. Evertz, A. Wokaun, F. N. Büchi, *J. Electrochem. Soc.* **2006**, *153*, A2158 – A2165.
[31] D. Candusso, J. P. Poirot-Rouvezier, B. Bador, E. Rulliere, R. Soulier, J. Y. Voyant, *Euro. Phys. J. Appl. Phys.* **2004**, *25*, 67 – 74.
[32] K. H. Hauer, R. Potthast, T. Wuster, D. Stolten, *J. Power Sources* **2005**, *143*, 67 – 74.
[33] D. J. L. Brett, S. Atkins, N. P. Brandon, V. Vesovic, N. Vasileiadis, A. R. Kucernak, *Electrochem. Commun.* **2001**, *3*, 628 – 632.
[34] P. C. Ghosh, T. Wuster, H. Dohle, N. Kimiaie, J. Mergel, D. Stolten, *J. Fuel Cell Sci. Technol.* **2006**, *3*, 351 – 357.
[35] Z. X. Liu, Z. Q. Mao, B. Wu, L. S. Wang, V. M. Schmidt, *J. Power Sources* **2005**, *141*, 205 – 210.
[36] F. N. Buchi, A. B. Geiger, R. P. Neto, *J. Power Sources* **2005**, *145*, 62 – 67.
[37] N. Rajalakshmi, M. Raja, K. S. Dhathathreyan, *J. Power Sources* **2002**, *112*, 331 – 336.
[38] P. Berg, K. Promislow, J. Stumper, B. Wetton, *J. Fuel Cell Sci. Technol.* **2005**, *2*, 111 – 120.
[39] Z. X. Liu, L. Z. Yang, Z. Q. Mao, W. L. Zhuge, Y. J. Zhang, L. S. Wang, *J. Power Sources* **2006**, *157*, 166 – 176.
[40] J. R. Selman, Y. P. Lin, *Electrochim. Acta* **1993**, *38*, 2063 – 2073.
[41] A. Parthasarathy, B. Dave, S. Srinivasan, A. J. Appleby, C. R. Martin, *J. Electrochem. Soc.* **1992**, *139*, 1634 – 1641.
[42] V. A. Paganin, C. L. F. Olivaira, E. A. Ticianelli, T. E. Springer, E. R. Gonzalez, *Electrochim. Acta* **1998**, *43*, 3761 – 3766.
[43] T. E. Springer, T. A. Zawodzinski, M. S. Wilson, S. Gottesfeld, *J. Electrochem. Soc.* **1996**, *143*, 587 – 599.
[44] J. P. Diard, B. Le Gorrec, C. Montella, C. Poinsignon, G. Vitter, *J. Power Sources* **1998**, *74*, 244 – 245.
[45] N. Wagner, W. Schnurnberger, B. Müller M. Lang, *Electrochim. Acta* **1998**, *43*, 3785 – 3793.
[46] J. M. Song, S. Y. Cha, W. M. Lee, *J. Power Sources* **2001**, *94*, 78 – 84.
[47] J. T. Mueller, P. M. Urban, *J. Power Sources* **1998**, *75*, 139 – 143.
[48] M. Eikerling, A. A. Kornyshev, *J. Electroanal. Chem.* **1999**, *475*, 107 – 123.
[49] D. J. L. Brett, S. Atkins, N. P. Brandon, V. Vesovic, N. Vasileiadis, A. Kucernak, *Electrochem. Solid-State Lett.* **2003**, *6*, A63 – A66.
[50] A. Hakenjos, C. Hebling, *J. Power Sources* **2005**, *145*, 307 – 311.
[51] I. A. Schneider, D. Kramer, A. Wokaun, G. G. Scherer, *Electrochem. Commun.* **2005**, *7*, 1393 – 1397.
[52] G. Hinds, M. Stevens, J. Wilkinson, M. de Podesta, S. Bell, *J. Power Sources* **2009**, *186*, 52 – 57.
[53] M. Eikerling, A. A. Kornyshev, A. R. Kucernak, *Phys. Today* **2006**, *59*, 38 – 44.
[54] R. Mosdale, G. Gebel, M. Pineri, *J. Membr. Sci.* **1996**, *118*, 269 – 277.
[55] R. J. Bellows, M. Y. Lin, M. Arif, A. K. Thompson, D. Jacobson, *J. Electrochem. Soc.* **1999**, *146*, 1099 – 1103.
[56] D. Kramer, J. B. Zhang, R. Shimoi, E. Lehmann, A. Wokaun, K. Shinohara, G. G. Scherer, *Electrochim. Acta* **2005**, *50*, 2603 – 2614.
[57] I. A. Schneider, D. Kramer, A. Wokaun, G. G. Scherer, *Electrochem. Commun.* **2005**, *7*, 1393 – 1397.
[58] J. B. Zhang, D. Kramer, R. Shimoi, Y. Ona, E. Lehmann, A. Wokaun, K. Shinohara, G. G. Scherer, *Electrochim. Acta* **2006**, *51*, 2715 – 2727.
[59] N. Pekula, K. Heller, P. A. Chuang, A. Turhan, M. M. Mench, J. S. Brenizer, K. Unlu, *Nucl. Instrum. Methods Phys. Res. Sect. A* **2005**, *542*, 134 – 141.
[60] A. Turhan, K. Heller, J. S. Brenizer, M. M. Mench, *J. Power Sources* **2006**, *160*, 1195 – 1203.
[61] J. J. Kowal, A. Turhan, K. Heller, J. Brenizer, M. M. Mench, *J. Electrochem. Soc.* **2006**, *153*, A1971 – A1978.
[62] R. Satija, D. L. Jacobson, M. Arif, S. A. Werner, *J. Power Sources* **2004**, *129*, 238 – 245.
[63] Y. P. Patil, T. A. P. Seery, M. T. Shaw, R. S. Parnas, *Ind. Eng. Chem. Res.* **2005**, *44*, 6141 – 6147.
[64] S. Basu, M. W. Renfro, H. Gorgun, B. M. Cetegen, *J. Power Sources* **2006**, *159*, 987 – 994.
[65] S. Basu, M. W. Renfro, B. M. Cetegen, *J. Power Sources* **2006**, *162*, 286 – 293.
[66] A. Panchenko, H. Dilger, J. Kerres, M. Hein, A. Ullrich, T. Kaz, E. Roduner, *Phys. Chem. Chem. Phys.* **2004**, *6*, 2891 – 2894.
[67] I. Tkach, A. Panchenko, T. Kaz, V. Gogel, K. A. Friedrich, E. Roduner, *Phys. Chem. Chem. Phys.* **2004**, *6*, 5419 – 5426.
[68] H. Matic, A. Lundblad, G. Lindbergh, P. Jacobsson, *Electrochem. Solid-State Lett.* **2005**, *8*, A5 – A7.
[69] K. W. Feindel, S. H. Bergens, R. E. Wasylishen, *J. Am. Chem. Soc.* **2006**, *128*, 14192 – 14199.
[70] S. Tsushima, K. Teranishi, S. Hirai, *Electrochem. Solid-State Lett.* **2004**, *7*, A269 – A272.
[71] K. Teranishi, S. Tsushima, S. Hirai, *J. Electrochem. Soc.* **2006**, *153*, A664 – A668.
[72] S. Tsushima, K. Teranishi, K. Nishida, S. Hirai, *Magn. Reson. Imaging* **2005**, *23*, 255 – 258.
[73] M. M. Mench, Q. L. Dong, C. Y. Wang, *J. Power Sources* **2003**, *124*, 90 – 98.
[74] K. Tüber, D. Pocza, C. Hebling, *J. Power Sources* **2003**, *124*, 403 – 414.
[75] P. Argyropoulos, K. Scott, W. M. Taama, *Electrochim. Acta* **1999**, *44*, 3575 – 3584.
[76] A. Su, F. B. Weng, C. Y. Hsu, Y. M. Chen, *Int. J. Hydrogen Energy* **2006**, *31*, 1031 – 1039.
[77] S. H. Ge, C. Y. Wang, *Electrochem. Solid-State Lett.* **2006**, *9*, A499 – A503.
[78] G. Q. Lu, C. Y. Wang, *J. Power Sources* **2004**, *134*, 33 – 40.

[79] H. Yang, T. S. Zhao, Q. Ye, *J. Power Sources* **2005**, *39*, 79 – 90.
[80] J. Martin, P. Oshkai, N. Djilali, *J. Fuel Cell Sci. Technol.* **2005**, *2*, 70 – 80.
[81] S. Y. Yoon, J. W. Ross, M. M. Mench, K. V. Sharp, *J. Power Sources* **2006**, *160*, 1017 – 1025.
[82] M. Wilkinson, M. Blanco, E. Gu, J. J. Martin, D. P. Wilkinson, J. J. Zhang, H. Wang, *Electrochem. Solid-State Lett.* **2006**, *9*, A507 – A511.
[83] D. Kim, J. Lee, T. H. Lim, I.-H. Oh, H. Y. Ha, *J. Power Sources* **2006**, *155*, 203 – 212.
[84] S. He, M. M. Mench, S. Tadigadapa, *Sens. Actuators A* **2006**, *125*, 170 – 177.
[85] A. Hakenjos, H. Muenter, U. Wittstadt, C. Hebling, *J. Power Sources* **2004**, *131*, 213 – 216.
[86] M. Wang, H. Guo, C. Ma, *J. Power Sources* **2006**, *157*, 181 – 187.
[87] D. J. L. Brett, A. R. Kucernak, S. Atkins, R. Blewitt, N. P. Brandon, B. P. Ladewig, J. Shrimpton, N. Vasileiadis, V. Vesovic in *Progress in Fuel Cell Research* (Ed.: P. V. Alemo), Nova, New York, **2007**, pp. 1 – 53.
[88] N. Vasileiadis, D. J. L. Brett, V. Vesovic, A. R. Kucernak, E. Fontes, N. P. Brandon, *J. Fuel Cell Sci. Technol.* **2007**, *4*, 336 – 344.
[89] A. A. Kulikovsky, A. Kucernak, A. A. Kornyshev, *Electrochim. Acta* **2005**, *50*, 1323 – 1333.
[90] D. J. L. Brett, N. P. Brandon, *J. Fuel Cell Sci. Technol.* **2007**, *4*, 29 – 44.
[91] E. Hontañón, M. J. Escudero, C. Bautista, P. L. Garcia-Ybarra, L. Daza, *J. Power Sources* **2000**, *86*, 363 – 368.
[92] A. Kumar, R. G. Reddy, *J. Power Sources* **2003**, *113*, 11 – 18.
[93] A. C. West, T. F. Fuller, *J. Appl. Electrochem.* **1996**, *26*, 557 – 565.
[94] X. G. Li, M. Sabir, *Int. J. Hydrogen Energy* **2005**, *30*, 359 – 371.
[95] P. L. Hentall, J. B. Lakeman, G. O. Mepsted, P. L. Adcock, J. M. Moore, *J. Power Sources* **1999**, *80*, 235 – 241.
[96] D. J. L. Brett, S. Atkins, N. P. Brandon, V. Vesovic, N. Vasileiadis, A. R. Kucernak, *J. Power Sources* **2007**, *172*, 2 – 13.
[97] D. J. L. Brett, S. Atkins, N. P. Brandon, V. Vesovic, N. Vasileiadis, A. R. Kucernak, *J. Power Sources* **2004**, *133*, 205 – 213.
[98] D. Brett, P. Aguiar, N. P. Brandon, A. Kucernak, *Int. J. Hydrogen Energy* **2007**, *32*, 863 – 871.
[99] F. Durst, A. Melling, J. H. Whitelaw, *Principles and practice of laser-Doppler anemometry*, Academic Press, London, **1976**.
[100] G. S. Beavers, D. D. Joseph, *J. Fluid Mech.* **1967**, *30*, 197 – 207.
[101] J. Martin, P.Oshkai, N. Djilali, *Proceedings of The Second International Conference on Fuel Cell Science Engineering and Technology*, Rochester, NY, **2004**, 595 – 602.
[102] D. Brett, P. Aguiar, R. Clague, A. Marquis, S. Schöttl, R. Simpson, N. P. Brandon, *J. Power Sources* **2007**, *166*, 112 – 119.
[103] R. Clague, D. J. L. Brett, P. Aguiar, A. J. Marquis, N. P. Brandon, *ECS Trans.* **2007**, *5*, 521 – 532.
[104] G. Hinds, *Reference electrodes for solid polymer fuel cells: a review*. NPL Report, **2008**.
[105] G. J. Offer, J. I. Golbert, P. Shearing, D. J. L. Brett, A. Atkinson, N. P. Brandon, *Electrochim. Acta* **2008**, *53*, 7614 – 7621.
[106] M. Pomfret, J. Owrutsky, R. Walker, *J. Phys. Chem. B* **2006**, *110*, 17305 – 17308.
[107] M. Pomfret, J. Owrutsky, R. Walker, *Anal. Chem.* **2007**, *79*, 2367 – 2372.
[108] M. B. Pomfret, J. Marda, G. S. Jackson, B. W. Eichhorn, A. M. Dean, R. A. Walker, *J. Phys. Chem. C* **2008**, *112*, 5232 – 5240.
[109] R. C. Maher, L. F. Cohen, P. Lohsoontorn, D. J. L. Brett, N. P. Brandon, *J. Phys. Chem. A* **2008**, *112*, 1497 – 1501.
[110] M. Mogensen, N. M. Sammes, G. A. Tompett, *Solid State Ionics* **2000**, *129*, 63 – 94.
[111] R. Körner, M. Ricken, J. Nötling, I. Riess, *J. Solid State Chem.* **1989**, *78*, 136 – 147.
[112] N. P. Brandon, D. J. L. Brett, *Philos. Trans. R. Soc. London Ser. A* **2006**, *364*, 147 – 159.
[113] J. R. Wilson, W. Kobsiriphat, R. Mendoza, H.-Y. Chen, J. M. Hiller, D. J. Miller, K. Thornton, P. W. Voorhees, S. B. Adler, S. A. Barnett, *Nat. Mater.* **2006**, *5*, 541 – 544.
[114] H. Iwai, N. Shikazono, T. Matsui, H. Teshima, M. Kishimoto, R. Kishida, D. Hayashi, K. Matsuzaki, D. Kanno, M. Saito, H. Muroyama, K. Eguchi, N. Kasagi, H. Yoshida, *J. Power Sources* **2009**, *195*, 955 – 961.
[115] P. S. Jorgensen, K. V. Hansen, R. Larsen, J. R. Bowen, *A Framework for Automatic Segmentation in Three Dimensions of Microstructural Tomography Data*, RISO National Laboratory for Sustainable Energy, Roskilde, **2009**.
[116] K. Matsuzaki, D. Kanno, H. Teshima, N. Shikazono, N. Kasagi, *Three-Dimensional Numerical Simulation of Ni-YSZ Anode Polarization Using Reconstructed Microstructure from FIB-SEM Images*, in SOFC-XI, Vienna, **2009**.
[117] B. Ruger, J. Joos, A. Weber, T. Carraro, E. Iver-Tiffee, *3D Electrode Microstructure Reconstruction and Modelling*. in SOFC-XI, Vienna, **2009**.
[118] J. R. Wilson, M. Gameiro, K. Mischaikow, W. Kalies, P. W. Voorhees, S. A. Barnett, *Microsc. Microanal.* **2009**, *15*, 71 – 77.
[119] D. Gostovic, J. R. Smith, D. P. Kundinger, K. S. Jones, E. D. Wachsman, *Electrochem. Solid-State Lett.* **2007**, *10*, B214 – B217.
[120] J. R. Smith, A. Chen, D. Gostovic, D. Hickey, D. Kundinger, K. L. Duncan, R. T. DeHoff, K. S. Jones, E. D. Wachsman, *Solid State Ionics* **2009**, *180*, 90 – 98.
[121] J. R. Wilson, J. S. Cronin, A. T. Duong, S. Rukes, H-Y Chen, K. Thornton, D. R. Mumm, S. Barnett, *J. Power Sources* **2009**, *195*, 1829 – 1840.
[122] J. R. Wilson, A. T. Duong, M. Gameiro, H-Y Chen, K. Thornton, D. R. Mumm, S. A. Barnett, *Electrochem. Commun.* **2009**, *11*, 1052 – 1056.
[123] J. R. Izzo, A. S. Joshi, K. N. Grew, W. K. S. Chiu, A. Tkachuk, S. H. Wang, W. Yun, *J. Electrochem. Soc.* **2008**, *155*, B504 – B508.
[124] P. R. Shearing, D. J. L. Brett, N. P. Brandon, *Int. Mater. Rev.* **2010**, DOI: 10.1179/095066010X12777205875679.
[125] J. I. Golbert, C. S. Adjiman, N. P. Brandon, *Ind. Eng. Chem. Res.* **2008**, *47*, 7693 – 7699.
[126] P. R. Shearing, Q. Cai, J. I. Golbert, V. Yufit, C. S. Adjiman, N. P. Brandon, *J. Power Sources* **2010**, *195*, 4804 – 4810.
[127] P. R. Shearing, J. Gelb, N. P. Brandon, *J. Eur. Ceram. Soc.* **2010**, *30*, 1809 – 1814.
[128] P. R. Shearing, J. I. Golbert, R. J. Chater, N. P. Brandon, *Chem. Eng. Sci.* **2009**, *64*, 3928 – 3933.
[129] X. Weng, Z. Zhang, D. Brett, V. Yufit, P. R. Shearing, M. Reece, H. Yan, J. A. Darr, *Solid State Ionics* **2010**, *181*, 827 – 834.
[130] U. Doraswami, P. Shearing, N. Droushiotis, K. Li, N. P. Brandon, G. H. Kelsall, *Solid State Ionics*, **2010**, DOI: 10.1016/j.ssi.2009.10.013.

Received: June 14, 2010
Revised: July 28, 2010
Published online on August 20, 2010

